A combined Finite Volumes -Finite Elements method for a low-Mach model

Caterina Calgaro, Claire Colin, Emmanuel Creusé

A combined Finite Volumes - Finite Elements method for a low-Mach model

Caterina Calgaro*, Claire Colin† and Emmanuel Creusé‡

December 14, 2018

Univ. Lille, CNRS, UMR 8524 - Laboratoire Paul Painlevé, F-59000 Lille, France.
and
INRIA Lille Nord Europe, EPI RAPSODI
Parc scientifique de la Haute Borne
40, avenue Halley - Bât A - Park Plaza
59650 Villeneuve d'Ascq, France.

Contents

*caterina.calgaro@univ-lille.fr, Corresponding author
†claire.lecerf@ed.univ-lille1.fr
‡emmanuel.creuse@univ-lille.fr

Abstract

In this paper, we develop a combined Finite Volumes - Finite Elements method based on a time splitting to simulate some low-Mach flows. The mass conservation equation is solved by a Vertex-Based Finite Volume scheme using a τ-limiter. The momentum equation associated with the compressibility constraint is solved by a Finite Element projection scheme. The originality of the approach is twofold. First, the state equation linking the temperature, the density and the thermodynamic pressure is imposed implicitly. Second, the proposed combined scheme preserves the constant states, in the same way as a similar one previously developed for the variable density Navier-Stokes system. Some numerical tests are performed to exhibit the efficiency of the scheme. On the one hand, academic tests illustrate the ability of the scheme in term of convergence rates in time and space. On the other hand, our results are compared to some of the literature by simulating a transient injection flow as well as a natural convection flow in a cavity.

Key Words: Low-Mach model, Finite Volume method, Finite Element method, Projection scheme.

1 Introduction

Variable density - low Mach numbers flows have been widely studied in the recent literature because of their applicability in various phenomena such as flows in high-temperature gas reactors, meteorological flows, flows with convective and/or conductive heat transfert, combustion processes and many others. In such cases, the resolution of the full compressible Navier-Stokes system is not adapted, because of the sound waves speed which is much faster than the entropy or the vorticity ones. Consequently, this choice would impose a too strong time-step limitation in the framework of explicit solvers, leading to unreachable numerical simulations. The Boussinesq incompressible model is not a better alternative for such low-speed phenomena. Indeed, the compressibility effects can not be totally canceled because of large variations of temperature and density, even if pressure ones are much smaller. Consequently, some models have been formally derived, leading to the filtering of the acoustic waves by the use of some formal asymptotic expansions [31, 28, 33, 38].

We recall that there exists two families of methods to compute flows at low-Mach number regime. On the one hand, there are the so-called density-based solvers, corresponding to methods used for the simulation of supersonic and transonic flows, which have been adapted to make them efficient and robust in the case of a low-Mach flow (see e.g. [22, 35, 36, 12, 23]) and references therein, using for example some preconditionning techniques [40, 30, 42, 41, 43]. On the other hand, there are the so-called pressure-based solvers, coming from the incompressible case. The pressure variations become independent from the state equation, and are coupled to the divergence condition on the velocity [10, 11]. In that case, considering the non-linearity of the coupled system, a fixed-point iterations process is usually performed, see e.g. [2, 13, 1]. A fractional step method, initially developed in [7, 8, 39] and progressively improved in [17, 18, 16, 19, 20] is used most of the time for the momentum equation. The pressure field comes from the resolution of a Poisson equation, for which the right-hand side contains some derivatives of the density or the temperature. Concerning the space discretization, lots of papers deal with Finite Element methods [24, 32], which can also been stabilized in the case of convection dominated regimes [37, 29, 13, 14, 1]. Others are also devoted to Finite Differences [34, 10, 27].

In this paper, we propose a combined Finite Volume - Finite Element method, which was initially developed for the simulation of incompressible and variable density flows [4]. This method is based on a time splitting allowing to solve the mass conservation equation by a Finite Volume method, and the momentum equation associated with the free divergence constraint on the velocity by a Finite Element one. It allows in particular to preserve the constant density states and to ensure the discrete maximum principle [3]. It also has been used to simulate some mixture flows such as avalanches [5]. Following the same philosophy, we propose to adapt this method to the case of a low-Mach model, providing a new pressure-based solver. The originality of our approach lies in the fact that the density is computed from the mass equation with a Finite Volume method, the other variables of the problem being approximated by a Finite Element method. In our work, the equation of state in not explicitly imposed. Moreover, the scheme recovers the properties of our previous proposed scheme at the incompressible limit, namely the preservation of the constant states, as well as the discrete maximum principle for the density.

The paper is organized as follows. In Section 2 the governing equations are recalled, and the choice of the final system to be solved is justified among several equivalent sets of equations. In Section 3, the combined Finite Volumes - Finite Elements is carefully described. Section 4 is devoted to some numerical simulations to exhibit the ability of the code. First, some analytical benchmarks are proposed and underline the accuracy of the scheme. Then, a transient injection flow [2, 14, 1] as well as the natural convection of a flow in a cavity [25, 24, 14, 1] are simulated.

2 Governing equations

2.1 Choice of the system

The equations modelling low Mach number flows are derived by inserting the asymptotic expansions of the variables with respect to the Mach number M in the Navier-Stokes compressible equations [31, 28, 10]. One of the characteristics of the process is that the pressure splits into two terms. Denoting $\mathbf{x} \in \mathbb{R}^d$ the space variable and $t \in \mathbb{R}_*^+$ the time one, we write:

$$p(\mathbf{x}, t) = P(t) + \pi(\mathbf{x}, t),$$

where P is called the thermodynamic pressure and π the dynamic pressure. P only depends on t, and π is in the order of M^2. The other variables considered are the velocity $\mathbf{u}(\mathbf{x}, t)$, the density $\rho(\mathbf{x}, t)$ and the temperature $T(\mathbf{x}, t)$. The non-dimensioned characteristic numbers of the flow are given by:

- The Mach number
$$\mathrm{M} = \frac{u_{ref}}{\sqrt{P_{ref}/\rho_{ref}}},$$
with u_{ref}, P_{ref} and ρ_{ref} some characteristic values for the velocity, the pressure and the density of the flow,

- The Reynolds number
$$\mathrm{Re} = \frac{u_{ref}\, l_{ref}\, \rho_{ref}}{\mu_{ref}},$$
with l_{ref} and μ_{ref} some characteristic length and viscosity,

- The Froude number
$$\mathrm{Fr} = \frac{u_{ref}}{\sqrt{g\, l_{ref}}},$$
with g the scalar-valued norm of the gravity field,

- The Prandtl number
$$\mathrm{Pr} = \frac{\mu_{ref}\, C_{P_{ref}}}{\lambda_{ref}},$$
with λ_{ref} and $C_{p_{ref}}$ characteristic values for the heat conductivity and the calorific capacity at constant pressure.

Moreover, assuming that the state law of the fluid is close to the one of a perfect case (see assumption 2.5. of [10]), a reference temperature of the flow is also deduced by

$$T_{ref} = \frac{P_{ref}}{C_{P_{ref}}\,\rho_{ref}}.$$

Finally, given α_{ref} a reference value for the compressibility coefficient at constant pressure, a non-dimensioned number β_{ref} is defined by:

$$\beta_{ref} = \alpha_{ref}\, T_{ref}.$$

According to single time scale and single space scale asymptotics, the continuity, momentum and temperature equations in the non-dimensioned formulation in an open polygonal domain $\Omega \subset \mathbb{R}^d$ are given by (see [28, 11], see also [10] adapted in case of a single-phase flow):

$$\begin{aligned} \frac{\partial \rho}{\partial t} + \nabla\cdot(\rho\mathbf{u}) &= 0, && (1)\\ \rho\left(\frac{\partial \mathbf{u}}{\partial t} + \mathbf{u}\cdot\nabla\mathbf{u}\right) + \nabla\pi - \frac{1}{\mathrm{Re}}\nabla\cdot\boldsymbol{\tau} &= -\frac{1}{\mathrm{Fr}^2}\,\rho\,\mathbf{e}_y, && (2)\\ \rho\, C_P\left(\frac{\partial T}{\partial t} + \mathbf{u}\cdot\nabla T\right) - \beta_{ref}\,\alpha\, T\,\frac{\mathrm{d}P}{\mathrm{d}t} - \frac{1}{\mathrm{Re}\,\mathrm{Pr}}\nabla\cdot(\lambda\nabla T) &= 0, && (3) \end{aligned}$$

where the density is obtained with the following equation of state:

$$\rho = \tilde{\rho}(T, P). \qquad (4)$$

Here, $\boldsymbol{\tau}$ is the viscosity stress tensor defined by

$$\boldsymbol{\tau} = \mu\left(\nabla\mathbf{u} + \nabla\mathbf{u}^{\mathrm{T}} - \frac{2}{3}\nabla\cdot\mathbf{u}\,\mathbf{I}\right),$$

where $\mu(T,P)$ is the fluid viscosity, $\lambda(T,P)$ the thermal conductivity and $\mathbf{e}_y = (0,1)^T$. The quantities $\alpha(T,P)$ and $C_P(T,P)$ are respectively the compressibility coefficient at constant pressure and the calorific capacity at constant pressure, in their non-dimensioned formulation. They are given by:

$$\alpha(T,P) = -\frac{1}{\beta_{ref}\,\rho}\frac{\partial\tilde{\rho}}{\partial T}(T,P), \qquad (5)$$

and

$$C_P(T,P) = \frac{\partial h}{\partial T}(T,P), \qquad (6)$$

where $h = e + \dfrac{P}{\rho}$ is the enthalpy of the fluid, and

$$e = \tilde{e}(T,P) \qquad (7)$$

is the internal energy. We assume that the equations of state (4) and (7) satisfy the thermodynamic hypothesis 3.2. given in [10], namely that there exists a strictly convex function $s(\frac{1}{\rho}, e)$, defined as the entropy of the fluid, verifying :

$$-T\,\mathrm{d}s = \mathrm{d}e + P\,\mathrm{d}\left(\frac{1}{\rho}\right).$$

This last assumption allows us to derive the equation (3) from the energy equation. Now, with the notation $\mathrm{D}_t = \dfrac{\partial}{\partial t} + \mathbf{u}\cdot\nabla$, using (4) in (1) and then (5), we obtain:

$$\nabla\cdot\mathbf{u} = \beta_{ref}\,\alpha\,D_t T - \frac{1}{\rho}\frac{\partial\tilde{\rho}}{\partial P}\frac{\mathrm{d}P}{\mathrm{d}t}.$$

Now the equation (3) takes the formulation:

$$\nabla\cdot\mathbf{u} = -\frac{1}{\Gamma P}\frac{\mathrm{d}P}{\mathrm{d}t} + \frac{\beta_{ref}\,\beta}{\mathrm{Re}\,\mathrm{Pr}\,P}\nabla\cdot(\lambda\nabla T), \tag{8}$$

where Γ is defined by

$$\Gamma(T,P) = \frac{\rho\,c^2}{P}(T,P), \tag{9}$$

$c = \sqrt{\dfrac{\partial\tilde{\rho}}{\partial P} - \dfrac{\beta_{ref}^2\,\alpha^2\,T}{C_P}}^{\,-1}$ being the sound velocity ; and β is defined by :

$$\beta(T,P) = \frac{\alpha\,P}{\rho\,C_P}(T,P). \tag{10}$$

Finally, the thermodynamic pressure time evolution is determined by integrating (8) over the domain $\Omega\subset\mathbb{R}^d$:

$$\frac{\mathrm{d}P}{\mathrm{d}t}\int_\Omega \frac{1}{\Gamma\,\beta_{ref}\,\beta} = -P\int_\Omega \frac{\nabla\cdot\mathbf{u}}{\beta_{ref}\,\beta} + \frac{1}{\mathrm{Re}\,\mathrm{Pr}}\int_{\partial\Omega}\lambda\,\nabla T\cdot\mathbf{n}, \tag{11}$$

where $\mathbf{n}$ is the outer unit normal to Ω on $\partial\Omega$.

In this work, we propose a new way to proceed, using the fact that the system (1)-(2)-(3)-(4)-(11) is equivalent to the system (1)-(2)-(3)-(8) and (11). In particular, we verify that the equation of state (4) is implicitly imposed. Indeed, starting from (1) and using (8) to subsitute the term $\nabla\cdot\mathbf{u}$, we get:

$$D_t\rho = -\rho\left(-\frac{1}{\Gamma\,P}\frac{\mathrm{d}P}{\mathrm{d}t} + \frac{\beta_{ref}\,\beta}{\mathrm{Re}\,\mathrm{Pr}\,P}\nabla\cdot(\lambda\nabla T)\right).$$

Now, using (3) to substitute the diffusive term gives :

$$D_t\rho = \left(\frac{\rho}{\Gamma\,P} + \frac{\beta_{ref}^2\,\rho\,\beta\,\alpha\,T}{P}\right)D_t P - \frac{\beta_{ref}\,\rho^2\,\beta\,C_P}{P}D_t T.$$

Finally, thanks to the expression of α, Γ and β respectively given in (5), (9) et (10), we obtain

$$D_t\rho = \frac{\partial\tilde{\rho}}{\partial P} D_t P + \frac{\partial\tilde{\rho}}{\partial T} D_t T.$$

Consequently, supposing that the equation of state is initially fulfilled, we can deduce (4).

Perfect gases. In most of applications (see for exemple [24, 26, 10, 2, 1, 14]), calorifically perfect gases are considered and we also restrict the rest of this work to the study of such fluids. For these gases, the equation of state in the dimensionless form[1] is given by

$$\rho = \frac{\gamma\, P}{(\gamma - 1)T}. \tag{12}$$

Consequently, $\alpha_{ref} = \dfrac{1}{T_{ref}}$ is a natural choice, and we get $\beta_{ref} = 1$. Thus we obtain:

$$C_P = 1, \quad \beta = \frac{\gamma - 1}{\gamma}, \quad c = \sqrt{(\gamma - 1)T}, \quad \Gamma = \gamma.$$

For the sake of simplicity, we also assume that the viscosity μ and the thermal conductivity λ are constant, namely $\lambda = \mu = 1$. We thus obtain the Navier-Stokes equations at low Mach number regime for a calorifically perfect gas:

$$\frac{\partial\rho}{\partial t} + \nabla\cdot(\rho\mathbf{u}) = 0, \tag{13}$$

$$\rho\left(\frac{\partial\mathbf{u}}{\partial t} + \mathbf{u}\cdot\nabla\mathbf{u}\right) + \nabla\pi - \frac{1}{\mathrm{Re}}\nabla\cdot\boldsymbol{\tau} = -\frac{1}{\mathrm{Fr}^2}\,\rho\,\mathbf{e}_y, \tag{14}$$

$$\rho\left(\frac{\partial T}{\partial t} + \mathbf{u}\cdot\nabla T\right) - \frac{\mathrm{d}P}{\mathrm{d}t} - \frac{1}{\mathrm{Re}\,\mathrm{Pr}}\Delta T = 0, \tag{15}$$

$$\nabla\cdot\mathbf{u} = -\frac{1}{\gamma P}\frac{\mathrm{d}P}{\mathrm{d}t} + \frac{\gamma - 1}{\gamma\,\mathrm{Re}\,\mathrm{Pr}\,P}\Delta T, \tag{16}$$

$$\frac{\mathrm{d}P}{\mathrm{d}t} = -\frac{\gamma\,P}{|\Omega|}\int_{\partial\Omega}\mathbf{u}\cdot\mathbf{n} + \frac{\gamma - 1}{|\Omega|\,\mathrm{Re}\,\mathrm{Pr}}\int_{\partial\Omega}\nabla T\cdot\mathbf{n}, \tag{17}$$

with

$$\boldsymbol{\tau} = \nabla\mathbf{u} + \nabla\mathbf{u}^{\mathrm{T}} - \frac{2}{3}\nabla\cdot\mathbf{u}\,\mathbf{I}.$$

[1] Denoting with star superscripts the dimensioned variables, the equations of states are defined with $\rho^* = \dfrac{P^*}{RT^*}$ and $e^* = \dfrac{RT^*}{\gamma - 1}$, where $\gamma = 1.4$ and $R = 287 Jkg^{-1}K^{-1}$ are the gas specific heat ratio and the gas constant, respectively. Then, we obtain $C_P^* = \dfrac{\gamma R}{\gamma - 1}$ and $\alpha^*(T^*) = \dfrac{1}{T^*}$.

2.2 Initial and boundary conditions

The initial conditions for the system (13)-(14)-(15)-(16) and (17) are given in Ω by:

$$\mathbf{u}(\mathbf{x},0) = \mathbf{u_0}(\mathbf{x}), \quad T(\mathbf{x},0) = T_0(\mathbf{x}), \quad P(0) = P_0, \quad \rho(\mathbf{x},0) = \frac{\gamma\, P_0}{(\gamma-1)T_0(\mathbf{x})}.$$

The boundary conditions on the velocity are given by:

$$\mathbf{u} = \mathbf{u}_D \quad \text{on } \partial\Omega,$$

where $\mathbf{u}_D$ is a function to be specified. We set $\overline{\partial\Omega} = \overline{\partial\Omega_D} \cup \overline{\partial\Omega_N}$ with $\partial\Omega_D \cap \partial\Omega_N = \emptyset$. We define $\mathbf{n}$ as the outward unit normal of Ω and $\partial\Omega_{in}$ the part of $\partial\Omega$ such that $\mathbf{u}_D \cdot \mathbf{n} < 0$. The boundary conditions on the temperature and density are respectively given by:

$$\left\{ \begin{array}{rcll} T & = & T_D & \text{on } \partial\Omega_D, \\ \nabla T \cdot \mathbf{n} & = & F_N & \text{on } \partial\Omega_N \end{array} \right.$$

and

$$\rho = \rho_{in} \text{ on } \partial\Omega_{in},$$

with T_D, F_N and ρ_{in} some functions to be specified.

3 The combined Finite Volumes - Finite Elements method

The combined Finite Volumes - Finite Elements scheme (C-FV-FE scheme) is based on a time splitting, allowing in particular to solve equation (13) by a finite volumes solver, and equations (14), (15), (16) by a finite elements one, using the same strategy as the one developed in [4] for the variable density incompressible Navier-Stokes system. We first describe the splitting used in time in order to reach the globally optimal accuracy in time according to the accuracy in time of each part of the scheme.

3.1 The time splitting

Let Δt be the time step and $t^n = n\Delta t$. Functions approximated at time t^n will be identified with superscript n. We assume that T^{n-1}, ρ^{n-1} and $\mathbf{u}^{n-1}$ as well as T^n, ρ^n and $\mathbf{u}^n$ are known approximated values.

1. Since we want at least the global mass conservation in the domain, the thermodynamic pressure P^{n+1} is computed by integrating the equation of state over Ω, using an extrapolation of the density and the temperature:

$$P^{n+1} = \frac{\gamma-1}{\gamma}\left(\int_\Omega 2\rho^n - \rho^{n-1}\right)\left(\int_\Omega \frac{1}{2T^n - T^{n-1}}\right)^{-1}. \tag{18}$$

2. The time derivative of the thermodynamic pressure $\left(\frac{\mathrm{d}P}{\mathrm{d}t}\right)^{n+1}$ is obtained through the use of equation (17) and an extrapolation of the temperature:

$$\begin{aligned}\left(\frac{\mathrm{d}P}{\mathrm{d}t}\right)^{n+1} + \frac{\gamma P^{n+1}}{|\Omega|}\int_{\partial\Omega} \mathbf{u}_D^{n+1}.\mathbf{n} &= \frac{\gamma-1}{|\Omega|\mathrm{Re}\,\mathrm{Pr}}\int_{\partial\Omega_D} \nabla(2T^n - T^{n-1})\cdot\mathbf{n} \\ &+ \frac{\gamma-1}{|\Omega|\mathrm{Re}\,\mathrm{Pr}}\int_{\partial\Omega_N} F_N^{n+1}. \end{aligned} \quad (19)$$

3. In order to ensure a local mass conservation in the domain, the density ρ^{n+1} at time t^{n+1} is computed by solving the continuity equation (13) using a second order Runge-Kutta scheme in time:

$$\frac{\hat{\rho}^{n+1}-\rho^n}{\Delta t} + \nabla\cdot(\rho^n\mathbf{u}^{n+\frac{1}{2}}) = 0, \quad (20)$$

$$\frac{\rho^{n+1}-\rho^n}{\Delta t} + \frac{1}{2}\left(\nabla\cdot(\rho^n\mathbf{u}^{n+\frac{1}{2}}) + \nabla\cdot(\hat{\rho}^{n+1}\mathbf{u}^{n+\frac{1}{2}})\right) = 0, \quad (21)$$

with

$$\mathbf{u}^{n+\frac{1}{2}} = \frac{(2\mathbf{u}^n - \mathbf{u}^{n-1}) + \mathbf{u}^n}{2} = \frac{3\mathbf{u}^n - \mathbf{u}^{n-1}}{2} \quad (22)$$

and

$$\hat{\rho}^{n+1} = \rho^{n+1} = \rho_{in}^{n+1} \text{ on } \partial\Omega_{in}. \quad (23)$$

4. The temperature T^{n+1} is computed by solving the temperature equation (15) using a BDF2-scheme in time:

$$\begin{aligned}\rho^{n+1}&\left(\frac{3T^{n+1}-4T^n+T^{n-1}}{2\,\Delta t} + (2\mathbf{u}^n - \mathbf{u}^{n-1})\cdot\nabla T^{n+1}\right) \\ &-\frac{3P^{n+1}-4P^n+P^{n-1}}{2\,\Delta t} - \frac{1}{\mathrm{Re}\,\mathrm{Pr}}\Delta T^{n+1} = 0 \end{aligned} \quad (24)$$

and

$$T^{n+1} = T_D^{n+1} \quad \text{on } \partial\Omega_D, \quad (25)$$

$$\nabla T^{n+1}\cdot\mathbf{n} = F_N^{n+1} \quad \text{on } \partial\Omega_N. \quad (26)$$

5. The velocity $\mathbf{u}^{n+1}$ and the pressure π^{n+1} are computed by solving the momentum equation (14) associated with the compressibility constraint (16) using a BDF2-scheme in time:

$$\begin{aligned}\rho^{n+1}&\left(\frac{3\mathbf{u}^{n+1}-4\mathbf{u}^n+\mathbf{u}^{n-1}}{2\,\Delta t} + (2\mathbf{u}^n - \mathbf{u}^{n-1})\cdot\nabla\mathbf{u}^{n+1}\right) + \nabla\pi^{n+1} \\ &-\frac{1}{\mathrm{Re}}\nabla\cdot\boldsymbol{\tau}^{n+1} = -\frac{1}{\mathrm{Fr}^2}\,\rho^{n+1}\,\mathbf{e}_y, \end{aligned} \quad (27)$$

$$\nabla\cdot\mathbf{u}^{n+1} = -\frac{1}{\gamma\,P^{n+1}}\left(\frac{\mathrm{d}P}{\mathrm{d}t}\right)^{n+1} + \frac{\gamma-1}{\gamma\,\mathrm{Re}\,\mathrm{Pr}\,P^{n+1}}\Delta(2T^n - T^{n-1}), \quad (28)$$

with

$$\nabla \cdot \boldsymbol{\tau}^{n+1} = \Delta \mathbf{u}^{n+1} + \frac{1}{3}\nabla\left(\nabla \cdot \mathbf{u}^{n+1}\right) \tag{29}$$

and

$$\mathbf{u}^{n+1} = \mathbf{u}_D^{n+1} \quad \text{on } \partial\Omega.$$

Similarly to other references [15, 20] or to our previous contributions for incompressible fluids [4, 5, 6], an extrapolation was used to approximate the convective velocity at time t^{n+1} by $2\mathbf{u}^n - \mathbf{u}^{n-1}$ in (24) and (27). Moreover, the velocity used in (20) and (21) is extrapolated at time $(t^n + t^{n+1})/2$ as indicated in (22), which is necessary to reach the second order accuracy. Note that in [4], alternatively to this extrapolation process, the second order in time was obtained thanks to a Strang splitting. Finally, an extrapolation of the temperature (and eventually of the density) was done in (18), (19) and (28). The choice $2T^n - T^{n-1}$ in (19) and (28) has to be the same for compatibility reasons, (19) being obtained by integrating (28) over Ω. We underline that with these choices, we did not observe any numerical instabilities. Following the same ideas as in [2, 13, 1], we also implemented a fixed-point method for the C-FV-FE scheme (see Appendix A for the description of the corresponding fixed-point algorithm), to evaluate its impact on some configurations (see section 4).

Remark 3.1. *As it will be explained in the next section, such a way to proceed allows in particular to solve the mass equation by a FV method. Consequently, it ensures a local mass conservation, while preserving the maximum principle on the density at the incompressible limit of the fluid. In that sense, the proposed numerical scheme can be seen as a generalization of the one previously developed for the variable density incompressible model [4].*

Remark 3.2. *Instead of solving equations* (18) *and* (19)*, we could compute* P^{n+1} *by solving the ordinary differential equation* (17) *using a BDF2-scheme in time, and approximate* $\left(\frac{\mathrm{d}P}{\mathrm{d}t}\right)^{n+1}$ *in* (28) *as made in* (24)*. However, although this strategy can be used for the simulation of evolutive smooth solutions, according to [25] we observe that for steady states this scheme can prevent the algorithm from reaching any stationary solution.*

Remark 3.3. *Instead of solving the temperature equation* (24)*, we could have in mind to use the state equation* (12) *to compute* T^{n+1}*. Nevertheless, this would lead to a lack of regularity of* T^{n+1}*, which is necessary in the constraint* (28) *in order to derive the values of* $\mathbf{u}^{n+1}$ *and* π^{n+1}*.*

3.2 Space discretization

The discretization in space is based on a triangulation of the domain $\Omega \subset \mathbb{R}^2$ by a set of triangles defining a regular mesh τ_h in the Ciarlet sense [9]. Each component of the velocity $\mathbf{u}_h$ is discretized by some $\mathbb{P}_2$-Lagrange finite elements, and the pressure π_h by some $\mathbb{P}_1$-Lagrange finite elements, leading to $H^1(\Omega)$ conforming approximations fulfilling the usual discrete LBB condition and consequently ensuring the stability of the discrete problem. The temperature T_h is also discretized by some $\mathbb{P}_2$-Lagrange finite elements, leading to a $H^1(\Omega)$ conforming approximation. The density ρ_h is discretized by piecewise constant values on a dual mesh τ_h^* associated with τ_h, allowing to consider a vertex-based finite-volume schemes for the resolution of the mass equation. The density field can also be interpreted as a $\mathbb{P}_1$-Lagrange finite elements field, since a value of the density is naturally associated with each node of any triangles. The degrees of freedom of each variable corresponding to the associated space discretization are displayed in Figure 1. For further details, we refer to [4].

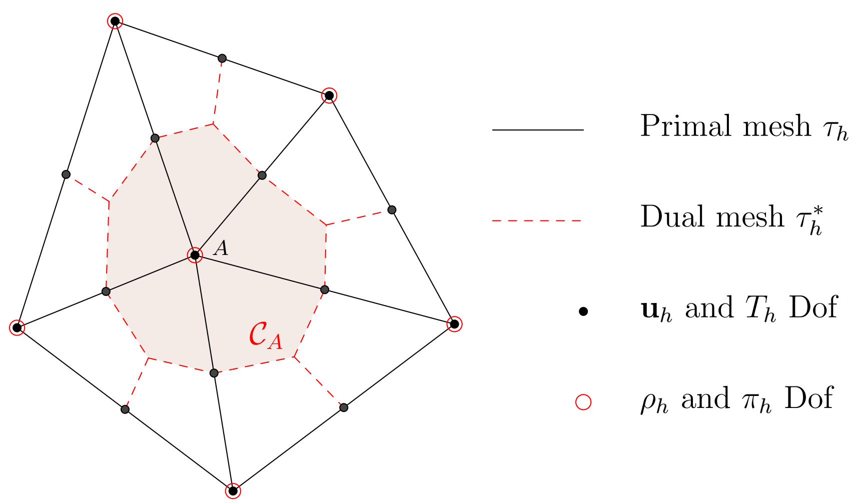

Figure 1: Space discretization: patch Ω_A. Meshes and Degrees of Freedom (DoF) for each variable.

3.2.1 Solving the thermodynamic pressure

Assuming that the approximated values of T_h^n, T_h^{n-1}, ρ_h^n and ρ_h^{n-1} are known, the values of P^{n+1} and $\left(\dfrac{\mathrm{d}P}{\mathrm{d}t}\right)^{n+1}$ are simply computed by using the discrete versions of (18) and (19), namely:

$$P^{n+1} = \frac{\gamma-1}{\gamma}\left(\int_\Omega 2\rho_h^n - \rho_h^{n-1}\right)\left(\int_\Omega \frac{1}{2T_h^n - T_h^{n-1}}\right)^{-1} \tag{30}$$

and

$$\left(\frac{\mathrm{d}P}{\mathrm{d}t}\right)^{n+1} + \frac{\gamma P^{n+1}}{|\Omega|}\int_{\partial\Omega} \mathbf{u}_D^{n+1}.\mathbf{n} = \frac{\gamma-1}{|\Omega|\mathrm{Re}\,\mathrm{Pr}}\int_{\partial\Omega_D} \nabla(2T_h^n - T_h^{n-1})\cdot\mathbf{n} + \frac{\gamma-1}{|\Omega|\mathrm{Re}\,\mathrm{Pr}}\int_{\partial\Omega_N} F_N^{n+1}. \tag{31}$$

3.2.2 Solving the temperature by a FE method

Assuming that ρ_h^{n+1}, T_h^n, T_h^{n-1}, $\tilde{\mathbf{u}}_h^n$, $\tilde{\mathbf{u}}_h^{n-1}$, P^{n+1}, P^n and P^{n-1} are known, the value of T_h^{n+1} is computed by the resolution of equation (24), namely:

$$\rho_h^{n+1}\left(\frac{3T_h^{n+1} - 4T_h^n + T_h^{n-1}}{2\,\Delta t} + (2\tilde{\mathbf{u}}_h^n - \tilde{\mathbf{u}}_h^{n-1})\cdot\nabla T_h^{n+1}\right) - \frac{3P^{n+1} - 4P^n + P^{n-1}}{2\,\Delta t} - \frac{1}{\mathrm{Re}\,\mathrm{Pr}}\Delta T_h^{n+1} = 0. \tag{32}$$

It is performed considering its weak finite elements formulation, associated with the boundary conditions specified in (25)-(26).

3.2.3 Solving the velocity by a FE method

We detail here the projection method used to derive $\mathbf{u}_h^{n+1}$ and π_h^{n+1}, contrary to [4] in which an Uzawa solver was considered. It constitutes a natural adaptation from the section 4 of [19] to the low-Mach model case. We assume that ρ_h^{n+1}, π_h^n, P^{n+1}, P^n, P^{n-1} and T_h^{n+1} are known, as well as the auxiliary variables $\tilde{\mathbf{u}}_h^n$, $\tilde{\mathbf{u}}_h^{n-1}$, ϕ_h^n, and ϕ_h^{n-1} specific to the projection method (where $(\tilde{\mathbf{u}}_h^0, \phi_h^0)$ and $(\tilde{\mathbf{u}}_h^1, \phi_h^1)$ are initialized in the same way as in [19]). First, the velocity field $\tilde{\mathbf{u}}_h^{n+1}$ which does not fulfill the constraint (16) is computed by solving the weak finite elements formulation of the parabolic equation, based on a BDF2 integration scheme, similarly to [16]:

$$\left\{\begin{aligned} \rho_h^{n+1}\Big(\frac{3\tilde{\mathbf{u}}_h^{n+1} - 4\tilde{\mathbf{u}}_h^n + \tilde{\mathbf{u}}_h^{n-1}}{2\Delta t} &+ (2\tilde{\mathbf{u}}_h^n - \tilde{\mathbf{u}}_h^{n-1})\cdot\nabla\tilde{\mathbf{u}}_h^{n+1}\Big) \\ &+ \nabla\left(\pi_h^n + \frac{4}{3}\phi_h^n - \frac{1}{3}\phi_h^{n-1}\right) - \frac{1}{\mathrm{Re}}\nabla\cdot\tilde{\boldsymbol{\tau}}_{\boldsymbol{h}}^{\,n+1} = -\frac{1}{\mathrm{Fr}^2}\,\rho_h^{n+1}\,\mathbf{e}_y, \\ \tilde{\mathbf{u}}_h^{n+1}|_{\partial\Omega} &= \mathbf{u}_D^{n+1}, \end{aligned}\right. \tag{33}$$

with

$$\nabla\cdot\tilde{\boldsymbol{\tau}}_h^{n+1} = \Delta\tilde{\mathbf{u}}_h^{n+1} + \frac{1}{3}\nabla\left(\nabla\cdot(2\tilde{\mathbf{u}}_h^n - \tilde{\mathbf{u}}_h^{n-1})\right). \tag{34}$$

Comparing (29) and (34), we notice that an extrapolation is used because of the projection method, since the two velocity components are computed successively. Then, the pressure ${\pi_h}^{n+1}$ is defined by:

$$\pi_h^{n+1} = \pi_h^n + \phi_h^{n+1}.$$

Here, ϕ_h^{n+1} is the solution of the weak finite elements formulation of the elliptic equation given by:

$$\left\{\begin{array}{rcl}\nabla\cdot\left(\dfrac{1}{\overline{\rho}_h^{n+1}}\nabla\phi_h^{n+1}\right) = \dfrac{3}{2\Delta t}\Big(\nabla\cdot\tilde{\mathbf{u}}_h^{n+1} & + & \dfrac{1}{\gamma P^{n+1}}\left(\dfrac{\mathrm{d}P}{\mathrm{d}t}\right)^{n+1} \\ & - & \dfrac{(\gamma-1)}{\gamma\,\mathrm{Re}\,\mathrm{Pr}\,P^{n+1}}\Delta(2T_h^n - T_h^{n-1})\Big), \\ \nabla\phi_h^{n+1}\cdot\mathbf{n}|_{\partial\Omega} = 0, & & \end{array}\right. \tag{35}$$

where for any triangle $K\in\tau_h$ we define:

$$\frac{1}{\overline{\rho}_h^{n+1}|_K} = \frac{1}{3}\sum_{A_i\in K}\frac{1}{\rho_h^{n+1}(A_i)}, \tag{36}$$

with A_i the three vertices belonging to the triangle K.

Remark 3.4. *Note that the choice of* $\overline{\rho}_h^{n+1}|_K$ *given in* (36) *is not unique. Another possible definition for* $\overline{\rho}_h^{n+1}|_K$ *is*

$$\frac{1}{\overline{\rho}_h^{n+1}|_K} = \frac{3}{\sum\limits_{A_i\in K}\rho_h^{n+1}(A_i)}$$

and leads to similar results. The essential point is to define a constant density per triangle identically in (35), (37) *and* (40), *see remark 3.6.*

Finally $\mathbf{u}_h^{n+1}$ can be defined by:

$$\mathbf{u}_h^{n+1} = \tilde{\mathbf{u}}_h^{n+1} - \frac{2\,\Delta t}{3\,\overline{\rho}_h^{n+1}}\nabla\phi_h^{n+1}, \tag{37}$$

even if there is no need to evaluate it from the practical point of view, as mentioned in [16].

3.2.4 Solving the density with a FV method

Assuming that $\rho_h^n, \rho_h^{n-1}, \tilde{\mathbf{u}}_h^n, \tilde{\mathbf{u}}_h^{n-1}, \phi_h^n$ and ϕ_h^{n-1} are known, the value of ρ_h^{n+1} is computed by the resolution of the discrete version of equations (20)-(21), namely:

$$\begin{array}{rcl}\dfrac{\hat{\rho}_h^{n+1}-\rho_h^n}{\Delta t} + \nabla\cdot(\rho_h^n\mathbf{u}_h^{*,n+\frac{1}{2}}) & = & 0, \\ \dfrac{\rho_h^{n+1}-\rho_h^n}{\Delta t} + \dfrac{1}{2}\left(\nabla\cdot(\rho_h^n\mathbf{u}_h^{*,n+\frac{1}{2}}) + \nabla\cdot(\hat{\rho}_h^{n+1}\mathbf{u}_h^{*,n+\frac{1}{2}})\right) & = & 0,\end{array} \tag{38}$$

where

$$\mathbf{u}_h^{*,n+\frac{1}{2}}|_K = \frac{3\mathbf{u}_h^{*,n}|_K - \mathbf{u}_h^{*,n-1}|_K}{2} \tag{39}$$

is defined by

$$\mathbf{u}_h^{*,n}|_K = \frac{1}{|K|}\int_K \left(\tilde{\mathbf{u}}_h^n - \frac{2\,\Delta t}{3\,\overline{\rho}_h^n}\nabla\phi_h^n\right). \tag{40}$$

The Finite-Volume method is carefully detailed in [4], and its generalization to ensure the L^∞-stability in the case of incompressible flows with the use of the so-called τ-limiters is given in [3]. Here, we point out the fact that from the values of the velocity obtained by the Finite Element scheme, we need to deduce the values of an auxiliary velocity $\mathbf{u}_h^{*,n+\frac{1}{2}}$ at the interfaces of the density control volumes surrounding each node of the triangulation. These interfaces correspond to the dotted lines of the dual mesh τ_h^* displayed in Figure 1. Following the same strategy as in the incompressible case [4], this value has to be piecewise constant on each triangle K of the mesh τ_h.

Remark 3.5. *Definition* (39) *of* $\mathbf{u}_h^{*,n+\frac{1}{2}}|_K$ *allows to ensure that in the case of a constant flow density in space (and consequently also constant in temperature), the scheme preserves the constant states imposed in the continuous model by the incompressibility constraint. In other words, the weak divergence property in the sense of the Finite Element projection method is transferred to the Finite Volume method, as it was proved in the context of a direct resolution by an Uzawa solver in [4].*

Remark 3.6. *In the incompressible case, let us note that the developed scheme allows to preserve the constant states. Indeed, let assume the following properties:*

- *(H1)* $P^n = P^{n-1}$ *and* $\left(\frac{\mathrm{d}P}{\mathrm{d}t}\right)^n = 0$,
- *(H2)* $T_h^n = T_h^{n-1} = T_h^{n-2}$ *are constant in space,*
- *(H3)* $\rho_h^n = \rho_h^{n-1} = \rho_h^{n-2}$ *are constant in space,*
- *(H4)* $\int_{\partial\Omega} \mathbf{u}_D^{n+1}\cdot\mathbf{n} = 0$.

We want to prove that $T_h^{n+1} = T_h^n$ *and* $\rho_h^{n+1} = \rho_h^n$. *First,* (30) *and* (31) *with assumptions (H2), (H3) and (H4) lead to* $P^{n+1} = P^n$ *and* $\left(\dfrac{\mathrm{d}P}{\mathrm{d}t}\right)^{n+1} = 0$. *Then, the weak formulation of* (35) *at time* t^n *writes:*

$$\begin{aligned}
-\int_{\Omega_A} \frac{1}{\overline{\rho}_h^n}\nabla\phi_h^n\cdot\nabla\psi_A \;&= \frac{3}{2\Delta t}\quad\left(\int_{\Omega_A}\nabla\cdot\tilde{\mathbf{u}}_h^n\,\psi_A + \frac{1}{\gamma P^n}\left(\frac{\mathrm{d}P}{\mathrm{d}t}\right)^n\int_{\Omega_A}\psi_A\right.\\
&\qquad\left. + \frac{\gamma-1}{\gamma\,\mathrm{Re}\,\mathrm{Pr}\,P^n}\int_{\Omega_A}\nabla(2T_h^{n-1}-T_h^{n-2})\cdot\nabla\psi_A\right),
\end{aligned}$$

where ψ_A *is the* $\mathbb{P}_1$ *basis function associated to an internal node* A *and* Ω_A *is the support of* ψ_A *(see Figure 1). Assumptions (H1), (H2) and (H4) lead to:*

$$\int_{\Omega_A}\left(\tilde{\mathbf{u}}_h^n - \frac{2\Delta t}{3\,\overline{\rho}_h^n}\nabla\phi_h^n\right)\cdot\nabla\psi_A = 0,$$

and definition (37) *of* $\mathbf{u}_h^n$ *gives:*

$$\int_{\Omega_A} \mathbf{u}_h^n \cdot \nabla \psi_A = 0.$$

It is the analogous of relation (23) in [4], which allows to obtain:

$$\int_{\partial \mathcal{C}_A} \mathbf{u}_h^{*,n} \cdot \mathbf{n} = 0,$$

where $\mathcal{C}_A$ *is the FV control volume associated to node A. Then, (H3) leads to* $\rho_h^{n+1} = \rho_h^n$. *Finally, equation* (32), *assumptions (H1) and (H2) associated to the previous results give* $T_h^{n+1} = T_h^n$.

Note that (32) and (33) are both implicit schemes in time for the resolution of parabolic equations, so that they are not constrained by a CFL condition. The only explicit scheme in time is applied to the continuity equation (38), so that the time step is constrained by a CFL condition and proportional to $h/||\mathbf{u}||_{L^\infty}$, see [3]. In practice, if Δt does not satisfy this CFL condition, a smaller time step Δt_{FV} satisfying the CFL condition is defined and sub-steps are made in the finite volume scheme to compute the density.

4 Numerical simulations

4.1 Analytical Benchmarks

4.1.1 Constant states

We first want to illustrate the fact that for incompressible flows, if the density and the temperature are initially homogeneous, then they remain constant (see Remark 3.6). It was already done for the density in the case of the variable density incompressible system using an Uzawa solver (see [4]). To do this, we consider the following analytical solution:

$$\left\{ \begin{array}{rcl} \mathbf{u_{ex}}(x,y) & = & 4\begin{pmatrix} -y(x-1)^2(x+1)^2(y-1)(y+1) \\ x(y-1)^2(y+1)^2(x-1)(x+1) \end{pmatrix}, \\ \rho_{\text{ex}} & = & 1, \\ T_{\text{ex}} & = & \dfrac{\gamma}{\gamma - 1} \\ P_{\text{ex}} & = & 1, \\ \pi_{\text{ex}} & = & -\dfrac{y}{Fr^2}, \end{array} \right. \tag{41}$$

in the square domain $\Omega = [-1,1]^2$. A source term in the right-hand-side of equation (14) is consequently added to the gravity term. Dirichlet boundary conditions are prescribed for the temperature on the whole boundary (i.e. $\partial\Omega = \partial\Omega_D$). Since $\partial\Omega_{in} = \emptyset$, there is no need to specify the value of ρ at the boundary. Simulations are performed on unstructured meshes at $\mathrm{Re} = 1$, $\mathrm{Pr} = \gamma$ and $1/\mathrm{Fr}^2 = 9.81$ up to time $t_f = 1 = N\Delta t$ with $\Delta t = h_{max} = 0.0625$ and h_{max} the maximum space step of the mesh. We give in Table 1 the values of $\max\limits_{0\le n\le N} ||\rho_h^n - \rho_{\mathbf{ex}}||_{L^\infty(\Omega)}$ and $\max\limits_{0\le n\le N} ||T_h^n - T_{\mathbf{ex}}||_{L^\infty(\Omega)}$.

$\max\limits_{0\le n\le N} \lVert\rho_h^n - \rho_{\mathbf{ex}}\rVert_{L^\infty(\Omega)}$	$\max\limits_{0\le n\le N} \lVert T_h^n - T_{\mathbf{ex}}\rVert_{L^\infty(\Omega)}$
2.91e-13	1.02e-13

Table 1: Constant density case, errors in density and temperature.

We observe on Table 1 that the density and the temperature remain constant nearly to the machine error during the whole simulation time, as it can be seen at the final time t_f in Figure 2 on the mesh corresponding to $h_{max} = 0.0625$. The density local maximum error is located in the vicinity of the boundaries. Consequently, the scheme ensures the preservation of the constant values of density and temperature in the presence of a gravity field, in the case where the velocity field is divergence free.

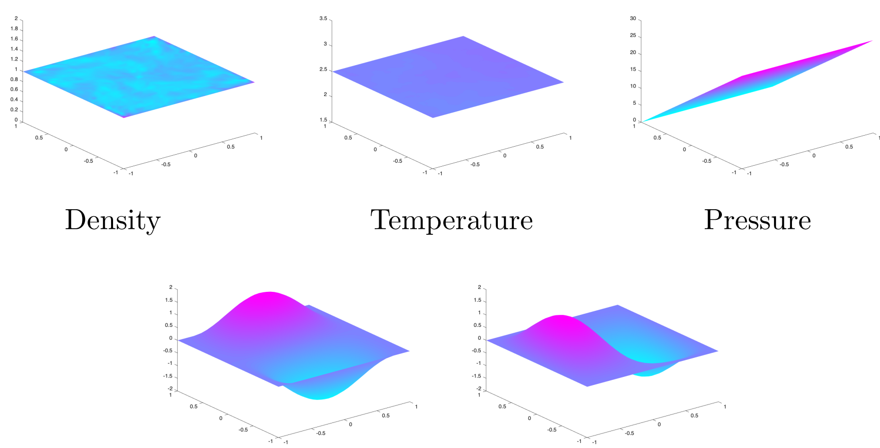

Figure 2: Density, temperature, pressure and the two velocity components at $t_f = 1$ for the mesh $h_{max} = 0.0625$.

4.1.2 Analytical solution

Now, in order to investigate the accuracy of the scheme, convergence tests are performed for a smooth solution and a non-solenoidal velocity field. The analytical solution is given by:

$$
\left\{
\begin{array}{rcl}
\mathbf{u}_{\mathbf{ex}}(t,x,y) & = & -\dfrac{1}{\gamma(2+\sin(2\pi t))}\left(\dfrac{2(\gamma-1)(2+\cos(2\pi t))}{(1+x^2+y^2)^2}+\pi\cos(2\pi t)\right)\begin{pmatrix} x \\ y \end{pmatrix}, \\
\rho_{\mathrm{ex}}(t,x,y) & = & \dfrac{\gamma(2+\sin(2\pi t))}{(\gamma-1)(2+\cos(2\pi t))}(1+x^2+y^2), \\
T_{\mathrm{ex}}(t,x,y) & = & \dfrac{2+\cos(2\pi t)}{1+x^2+y^2}, \\
P_{\mathrm{ex}}(t) & = & 2+\sin(2\pi t), \\
\pi_{\mathrm{ex}}(t,x,y) & = & \sin(x)\sin(y)\sin(2\pi t),
\end{array}
\right.
\tag{42}
$$

in the square $\Omega = [-1,1]^2$. The Reynolds and Prandtl numbers are both equal to 1, the gravity term is not considered and appropriated source terms are added in the right-hand-sides of equations (13), (14) and (15). Non-homogeneous Neumann boundary conditions on the temperature are prescribed on the whole boundary of Ω (i.e. $\partial\Omega = \partial\Omega_N$), so that $F_N = \nabla T_{ex} \cdot \mathbf{n}$ on $\partial\Omega$; and $\rho_{in} = \rho_{ex}$ on $\partial\Omega_{in} = \partial\Omega$.

The simulations are performed on unstructured grids in the range $1/150 \le h_{max} \le 1/50$, up to the final time $t_f = 0.2$, using $\Delta t = h_{max}$. In order to evaluate the performances of the splitting proposed in section 3.1, the C-FV-FE scheme results are compared with the ones obtained using some fixed-point iterations, see Appendix A. In that case, the fixed-point iterations are performed until the L^2-norm of two successive iterates is smaller than 10^{-10} for all variables. From the practical point of view, we observe that the fixed point converges in 6 or 7 iterations for the worst cases. Finally, these results are also compared to those obtained with one of the schemes proposed in [2] (pressure-based solver, asymptotic approach 1), for which some fixed-point iterations are required.

We observe, whatever the considered scheme, that the thermodynamic pressure P converges at order 2 in the $L^\infty(0,t_f)$ norm. We plot in Figure 3 the $L^\infty(0,t_f;L^2(\Omega))$ norm of the errors on the density ρ_h, the temperature T_h, the velocity $\mathbf{u}_h$ and the dynamic pressure π_h as a function of h_{max} in a log/log scale. On the one hand, all schemes provide a convergence rate at order 2 for the density, the temperature and the velocity. Concerning the dynamic pressure, a rate slightly larger than 1.5 is obtained. More precisely, for the C-FV-FE scheme, a rate between 1.65 and 1.85 is observed, as we can see in Table 2. These results are in good agreement with the incompressible constant density case, for which it was proved in [21] that the errors in time in the $L^2(\Omega)$-norm for the velocity and the pressure are of order 2 and 3/2 respectively. In fact, the numerical convergence rate obtained for the dynamic pressure is slightly better than the theorical expected one. On the other hand, we can see that the results obtained using the C-FV-FE scheme with or without a fixed–point iterations procedure correspond to the same orders of convergence. In particular, the errors are quite the same, except a small difference in the density error. In conclusion, the fixed-point iterations are not necessary for the C-FV-FE scheme on this analytical solution benchmark to obtain optimal convergence orders. We also point out that the fixed-point iterations are crucial

h_{max}	Error P	Rate	Error ρ	Rate	Error T	Rate	Error u	Rate	Error π	Rate
2.00e-2	5.12e-3	-	2.84e-3	-	3.31e-3	-	8.49e-4	-	6.44e-2	-
1.56e-2	3.31e-3	1.76	1.76e-3	1.94	2.13e-3	1.79	4.72e-4	2.38	4.29e-2	1.65
1.11e-2	1.74e-3	1.89	9.04e-4	1.95	1.06e-3	2.05	2.10e-4	2.38	2.38e-2	1.73
7.81e-3	8.95e-4	1.89	4.54e-4	1.96	5.48e-4	1.87	1.03e-4	2.02	1.26e-2	1.80
6.67e-3	6.53e-4	1.99	3.32e-4	1.97	3.87e-4	2.19	7.48e-5	2.02	9.39e-3	1.85

Table 2: C-FV-FE scheme. Errors in $L^\infty(0,t_f;L^2(\Omega))$ norm and corresponding convergence rates.

for the scheme proposed in [2]. Indeed, without the fixed–point iterations, the scheme does not converge for the dynamic pressure, and orders of convergence are smaller than one for the velocity and the temperature.

In Figure 4, we plot the $L^\infty(0,t_f;L^2(\Omega))$ error on the discrete state equation, defined by:

$$err_h = \max_{0\leq n\leq N} \left|\left|\rho_h^n - \frac{\gamma\, P^n}{(\gamma-1)T_h^n}\right|\right|^2_{L^2(\Omega)},$$

obtained with the C-FV-FE scheme. As explained in section 2.1, the state equation is imposed implicitly. As we can see, err_h converges towards zero at order 2, which corresponds to the expected behaviour because of the previous convergence rates obtained in ρ_h, T_h and P.

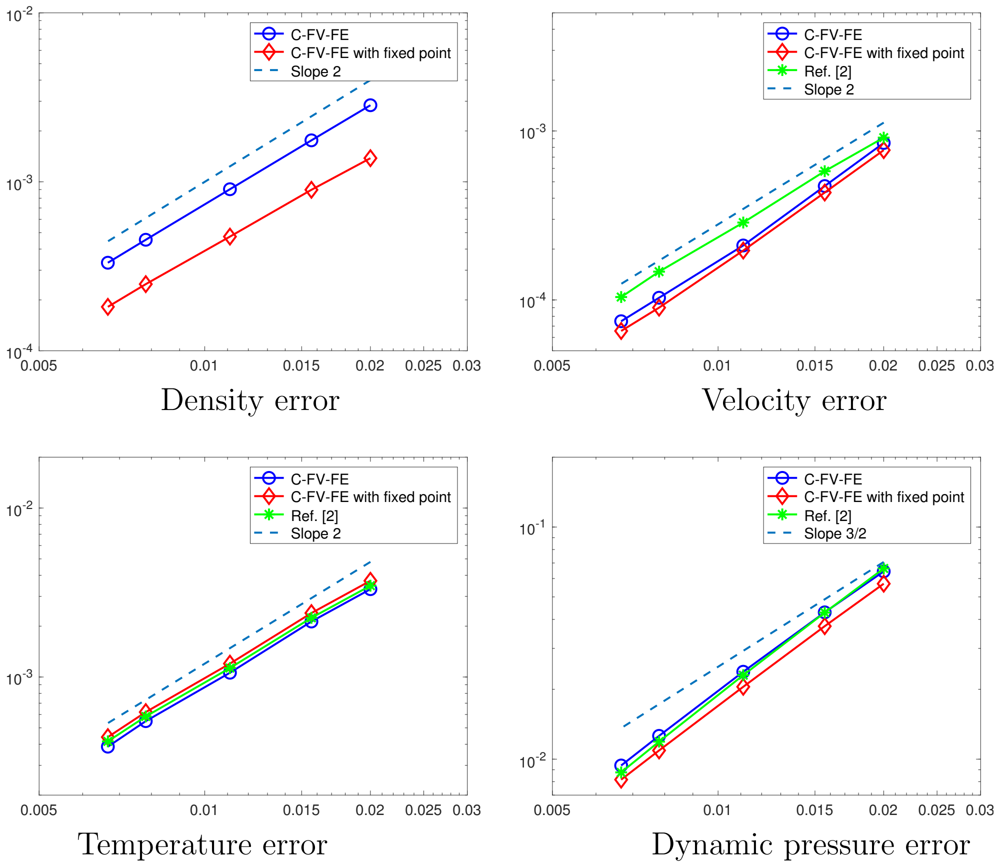

Figure 3: Errors in $L^\infty(0, t_f; L^2(\Omega))$ norm versus h_{max}, log/log scale.

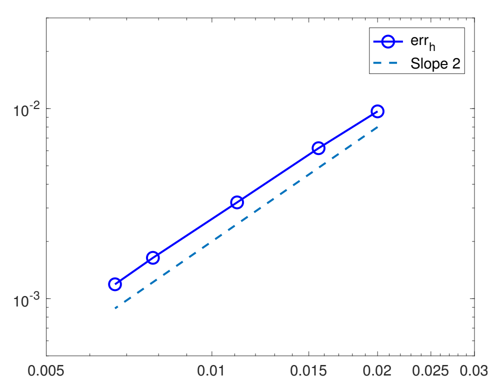

Figure 4: Error in $L^\infty(0, t_f; L^2(\Omega))$ norm on the discrete state equation versus h_{max}, C-FV-FE scheme, log/log scale.

4.2 The transient injection flow

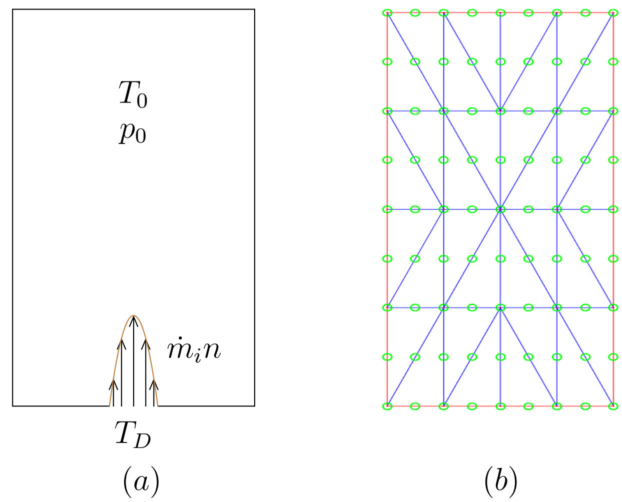

Figure 5: (a) : The cavity Ω. (b) : The grid mesh 4×4.

This benchmark was initially proposed in [2] and also considered in [14] and [1]. Considering the non-dimensioned equations, the domain is defined by a rectangle $\Omega = [-1.5\,;\,1.5] \times [0\,;\,7]$ (see Figure 5(a)), defining a cavity in which a calorifically perfect gas is initially at rest. The inital temperature and thermodynamic pressure values are given by:

$$T_0 = 300 \quad \text{and} \quad P_0 = 1. \tag{43}$$

The Reynolds, the Prandtl and the Froude numbers of the fluid are respectively equal to Re $= 40$, Pr $= 0.71$ and Fr $= 0.042$. Zero Dirichlet boundary conditions for the velocity and zero Neumann ones for the temperature are specified on all boundaries, except for a small hole in the bottom wall defined by $\partial\Omega_D = \partial\Omega_{in} = \left[-\dfrac{l}{2};\dfrac{l}{2}\right] \times \{0\}$, with $l = 0.2$:

$$\begin{aligned} \mathbf{u}(t,x,y)|_{\partial\Omega_N} &= \mathbf{0}, \\ \nabla T \cdot \mathbf{n}|_{\partial\Omega_N} &= 0. \end{aligned}$$

On $\partial\Omega_D$, the fluid is injected at the temperature $T_D = 600$, subject to a parabolic inflow profile. The momentum is imposed on $\partial\Omega_{in}$ from $t = 0$ up to $t_f = 6$ by:

$$(\rho\,\mathbf{u})_i n(x,y) = \left(0\,;\, \frac{6 \times 2.87 \cdot 10^{-3}\,\gamma\,\dot{m}_i n}{l^2\,(\gamma-1)} \left(\frac{l^2}{4} - x^2\right)\right)^T \quad \text{for } 0 \leq t \leq 6, \tag{44}$$

where $\dot{m}_i n = 1$ is the average momentum. Because of this kind of boundary condition, after the computation of P^{n+1} we update the velocity as follows:

$$\mathbf{u}_D^{n+1} = \left(0, \frac{2.87 \cdot 10^{-3}\, T_D}{P^{n+1}} \frac{6\, \dot{m}_i n}{l^2} \left(\frac{l^2}{4} - x^2\right)\right)^T = \left(0, \frac{258.3}{P^{n+1}} \left(\frac{l^2}{4} - x^2\right)\right)^T.$$

Note that in [14] and [1], different boundary conditions are considered. Consequently, the time evolution of the temperature is relatively similar but not exactly comparable with the results presented in [2]. If the boundary conditions given in [14] are enforced in the C-FV-FE scheme, we can observe analogous temperature distribution and velocity field as those presented in [14].

First of all, we check the grid convergence property. We use some structured meshes like the one displayed in Figure 5(b). We plot in Figure 6 the isovalues of the temperature at $t_f = 6$. Results are obtained on three meshes corresponding respectively to grids 60×60, 120×120 and 180×180, and using $\Delta t = h_{max}$. Even if the jet obtained with the 60×60 grid seems to be a little delayed, we can see by comparing the solutions obtained for grids 120×120 and 180×180 that they are close to each other.

Also, we plot in Figure 7 the evolution of the velocity components u_x and u_y and of the temperature T along the vertical lines $x = 0$, $x = -L/4$ and horizontal ones $y = H/4$, $y = H/2$ and $y = 3H/4$ at $t = 6$. The temperature distribution and the velocity field are nearly the same in both cases, so that the grid convergence can be considered as achieved. Let us note that although the shape of the cross-sections showed in Figure 7 are comparable to the profiles plotted in Figures 8 and 9 in [2], their amplitudes are slightly greater. These differences can be explained by the ability of our scheme to preserve locally the density of the fluid.

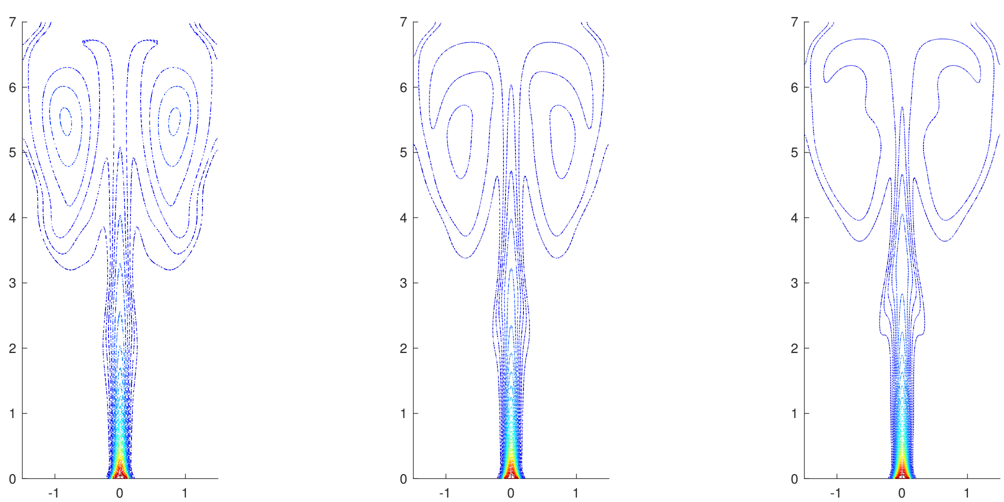

Figure 6: C-FV-FE scheme, temperature at $t = 6$. From the left to the right: Grids 60×60, 120×120 and 180×180. 40 isovalues from 330 to 600, uniform distribution.

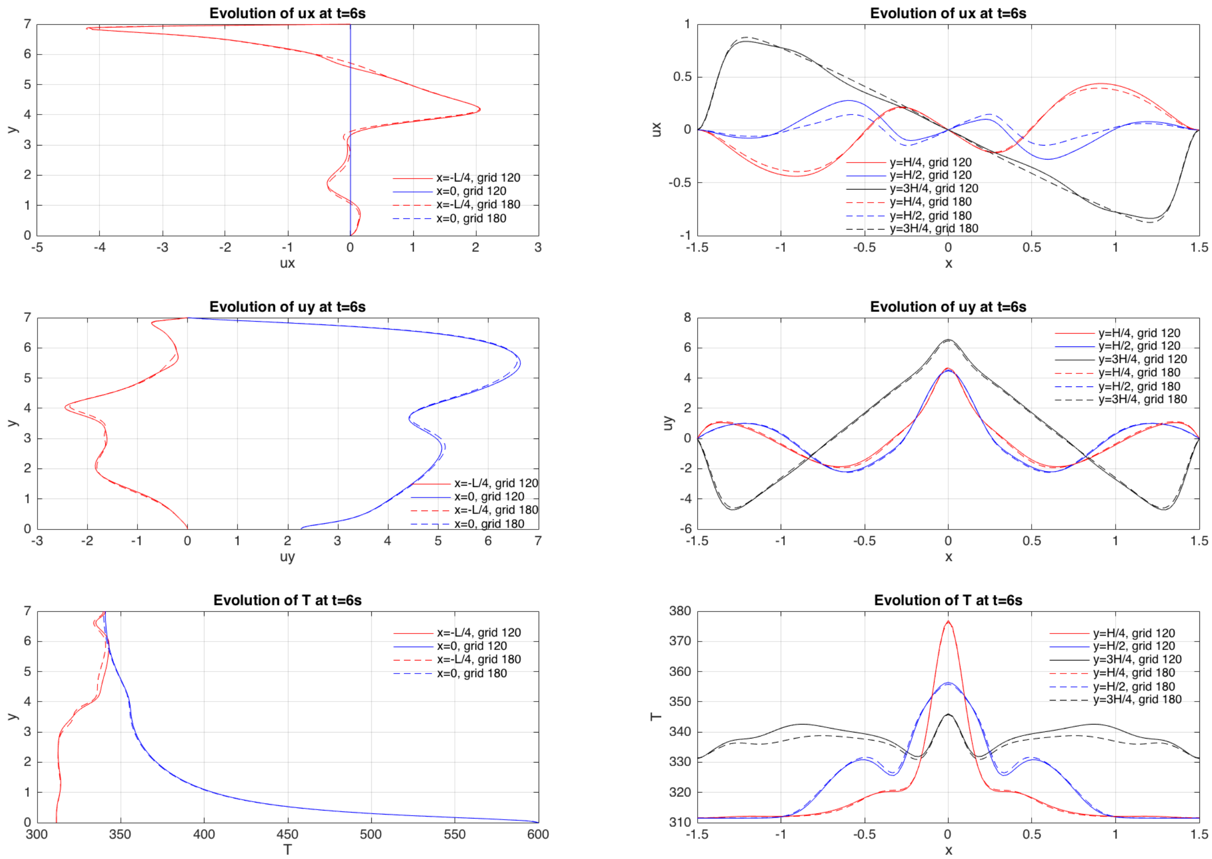

Figure 7: Evolution of u_x, u_y and T along the lines $x = 0$, $x = -L/4$, $y = H/4$, $y = H/2$ and $y = 3H/4$ at $t = 6$, for the grids 120×120 and 180×180.

In order to confirm the observations made in section 4.1.2, we compare in Figure 8 the temperature distributions obtained with the C-FV-FE scheme and with the scheme from [2] (pressure-based solver, asymptotic approach 1) at time $t_f = 6$ on a 120×120 grid, without and with the fixed-point process. In that second case, we require the relative error to be smaller than 10^{-10} for all variables, leading to about 15 iterations. We can first observe that with some fixed-point iterations, the propagation speed of the jet is very similar for the two schemes (compare (b) and (d)). Nevertheless, without the fixed-point iterations, this propagation speed is nearly the same for the C-FV-FE scheme (compare (a) and (b)), whereas the phenomenon is delayed for the other scheme (compare (c) and (d)), like observed in Figure 10 in [2].

Since the law state is imposed implicitly in the C-FV-FE scheme, we check in Figure 9(a) the convergence towards zero of the discrete state equation error in the $L^2(0, t_f; L^2(\Omega))$ norm. In any case (with or without fixed-point iterations), it goes towards zero, even if the convergence is faster with some fixed-point iterations.

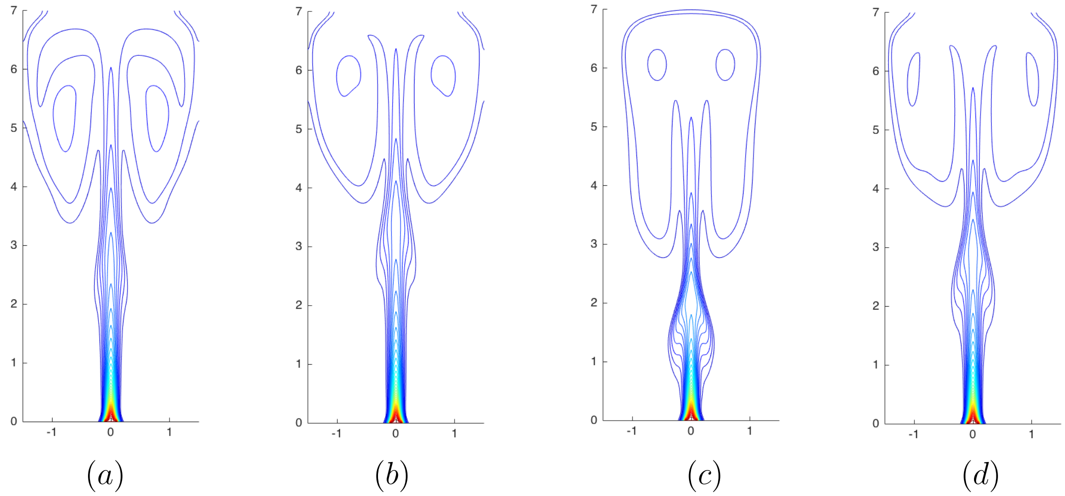

Figure 8: Temperature at $t = 6$. Comparison between C-FV-FE scheme and scheme in [2]. (a) : C-FV-FE scheme. (b) : C-FV-FE scheme with fixed-point iterations. (c) : scheme in [2] without fixed-point iterations. (d) : scheme in [2].

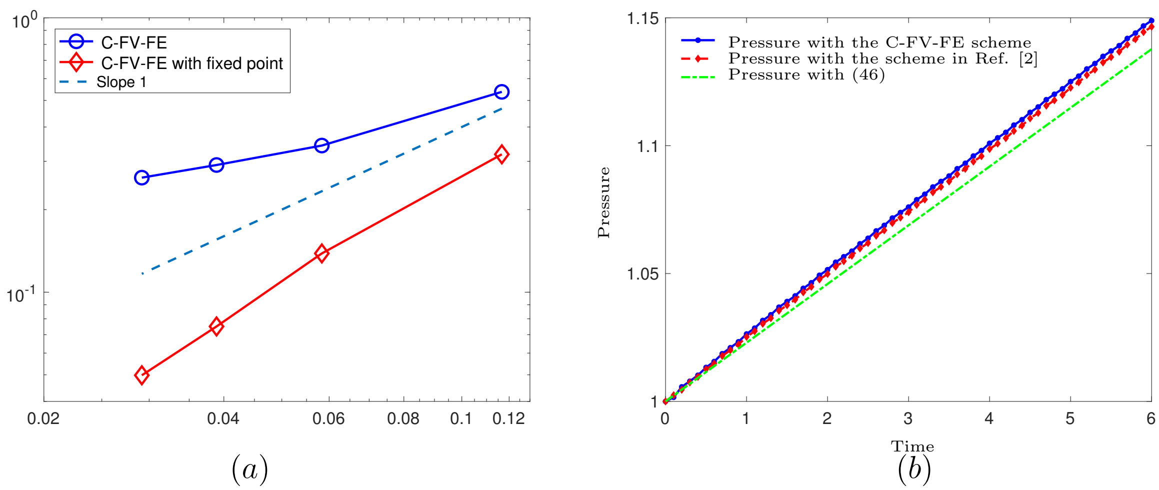

Figure 9: (a) : Error in $L^2(0, t_f; L^2(\Omega))$ norm on the discrete state equation versus h_{max}, log/log scale. (b) : Evolution of the thermodynamic pressure.

Finally, we want to investigate the thermodynamic pressure evolution. Similarly to [2], neglecting the diffusive term in (17), we get:

$$\frac{\mathrm{d}P}{\mathrm{d}t} + \frac{\gamma P}{|\Omega|} \int_{\partial\Omega} \mathbf{u}.\mathbf{n} \simeq 0. \tag{45}$$

Using the value of $(\rho\,\mathbf{u})_i n$ given in (44), and the state equation (12) to evaluate $\rho_i n$, we can explicitly solve (45) to obtain an approximation of the thermodynamic pressure:

$$P(t) \simeq P_0 + \frac{258.3\,\gamma}{750\,|\Omega|}\,t. \tag{46}$$

Figure 9(b) displays the evolution of the approximate thermodynamic pressure given by (46), the one computed with the C-FV-FE scheme and also by the scheme from [2] on a 120×120 grid. Once again, results are close to each other.

Remark 4.1. *In order to give a justification to the approximation used in the derivation of* (45)*, we computed the average values in time of* $\dfrac{\gamma P}{|\Omega|}\displaystyle\int_{\partial\Omega} \mathbf{u}.\mathbf{n}$ *and* $\dfrac{\gamma - 1}{|\Omega| Re\, Pr}\displaystyle\int_{\partial\Omega} \nabla T \cdot \mathbf{n}$ *with the C-FV-FE scheme, and obtained the values of* $2.26e-02$ *and* $4.62e-04$ *respectively. Consequently, as the second term is two orders of magnitude below the first one, here it can be neglected. This fact can also explain that the pressure given by* (46) *in slightly lower that the one computed using the C-FV-FE scheme, since the second term is not only very small, but also positive.*

4.3 The natural convection in a cavity

4.3.1 The original benchmark

This flow example has been proposed in [26] as a benchmark problem for natural convection flows with large temperature gradients. It was also considered in e.g. [24, 1, 14]. We consider a square cavity $\Omega = [0, 1]^2$ containing a calorifically perfect gas, see Figure

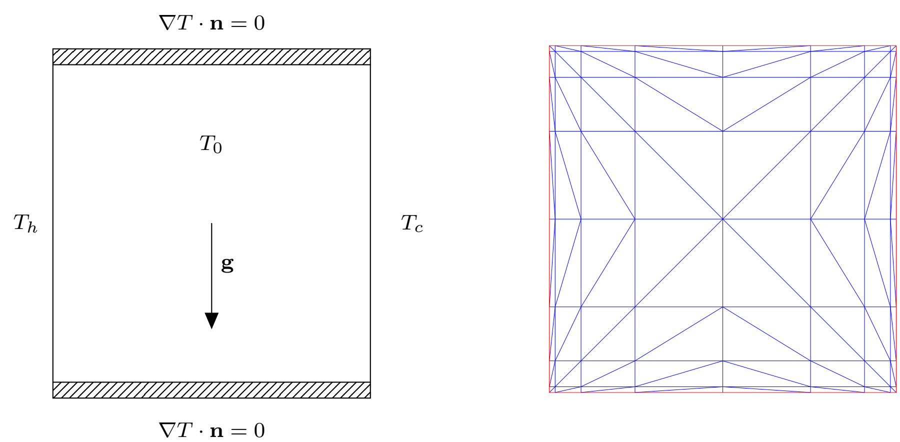

(a) (b)

Figure 10: (a) : The differentially heated cavity. (b) : The refined mesh.

10(a). The gas is initially at rest with uniform temperature and pressure :

$$\mathbf{u}_0 = \mathbf{0}\ m.s^{-1}, \quad T_0 = 600 \text{ K} \quad \text{and} \quad P_0 = 101325 \text{ Pa}.$$

On all walls, the no-slip condition is imposed for the velocity, namely :

$$\mathbf{u}|_{\partial\Omega} = \mathbf{0}, \text{ so that } \partial\Omega_{in} = \emptyset.$$

A temperature of $T_h = T_0(1+\varepsilon)$ (respectively $T_c = T_0(1-\varepsilon)$) is imposed on the left (respectively right) wall with $\varepsilon = 0.6$. The horizontal walls are insulated. Denoting by $\partial\Omega_N = [0,1]\times\{0,1\}$, we thus have :

$$\nabla T \cdot \mathbf{n}|_{\partial\Omega_N} \;=\; 0.$$

The Prandtl and Rayleigh numbers of the flow are respectively given by $\mathrm{Pr} = 0.71$ and

$$\mathrm{Ra} = \frac{2\,\varepsilon\,\mathrm{Pr}\,g\,l_{ref}^2}{\nu^2} = 10^6,$$

similarly to [24]. We are interested in the solution when the steady-state is reached. A quantity of interest for this benchmark is the Nusselt number, which represents the heat transfer from the hot to the cold wall. It is defined as:

$$\mathrm{Nu}(x,y) = \frac{l_{ref}}{T_h - T_c}\nabla T(x,y)\cdot\mathbf{n}, \quad \forall (x,y)\in\partial\Omega.$$

An average Nusselt number is computed on both hot and cold walls, and is respectively denoted by Nu_c and Nu_h. We also define

$$\mathrm{Nu}_{av} = \frac{\mathrm{Nu}_c + \mathrm{Nu}_h}{2}.$$

Finally, we are interested in the value of the ratio of thermodynamic pressure P over the initial pressure P_0, and in the difference between its value and the reference one.

Like in [24], meshes are defined by the number of segment N on each of the four boundaries of the domain. Moreover, they are refined in the vicinity of the boundaries using a geometrical progression and ensuring an aspect ratio (defined as the ratio of the length of the largest segment in the mesh over the length of the smallest one) equal to 15.1, see Figure 10(b) for an example in the case $N = 8$. At each time step, few fixed-point iterations are performed: we require the relative error on all the variables to decrease of four order of magnitude or, except in a very short interval of time $[0, t_s]$ (for instance $t_s = 10\Delta t$), we enforce at most two fixed-point iterations. Time iterations are performed until the relative residual on all the variables is less that 10^{-5}, leading to the numerical steady state. Let us note that the fixed-point iterations are here necessary to reach this steady state and to avoid some small oscillations on the velocity field.

The grid convergence study is given in Table 3, and the temperature and velocity fields are displayed for the mesh $N = 256$ in Figure 11. We can observe that each of the Nusselts numbers Nu_c and Nu_h goes towards its reference value when the mesh is being refined. The value of Nu_{av} goes towards zero and is divided by a factor four when the value of N is twice, as well as the value of $P/P_0 - (P/P_0)_{ref}$. We also check in Figure 12 the convergence towards zero of the discrete state equation in the $L^2(0, t_f; L^2(\Omega))$ norm, and observe a convergence rate around 0.5 when the mesh is being refined.

	Nu_c	Nu_h	Nu_{av}	P/P_0	$P/P_0 - (P/P_0)_{ref}$
Ref. values [24]	**8.85978**	**-8.85978**	**0**	**0.85633**	**0**
$N = 64$	8.87358	-8.98999	-0.1164	0.84769	-0.00864
$N = 96$	8.83670	-8.93469	-0.0980	0.84819	-0.00814
$N = 128$	8.83551	-8.86779	-0.0323	0.85375	-0.00258
$N = 192$	8.84402	-8.85730	-0.0133	0.85512	-0.00121
$N = 256$	8.85452	-8.86184	-0.0073	0.85564	-0.00069

Table 3: Heated cavity, $\varepsilon = 0.6$ and $Ra = 10^6$.

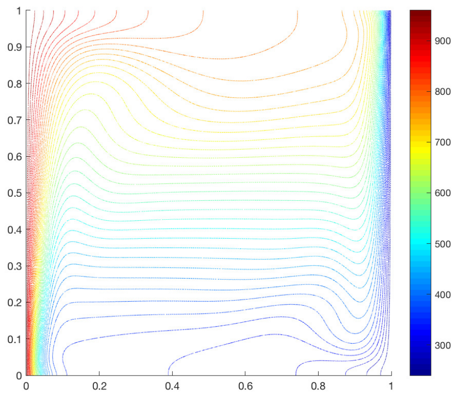

Temperature

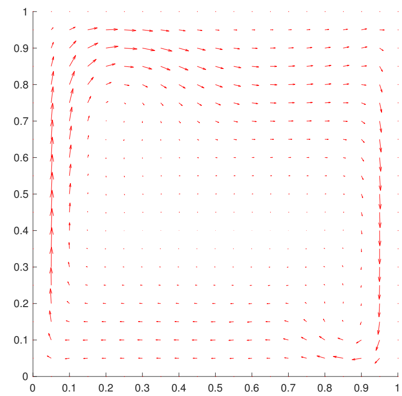

Velocity field

Figure 11: Temperature and velocity field for the mesh $N = 256$.

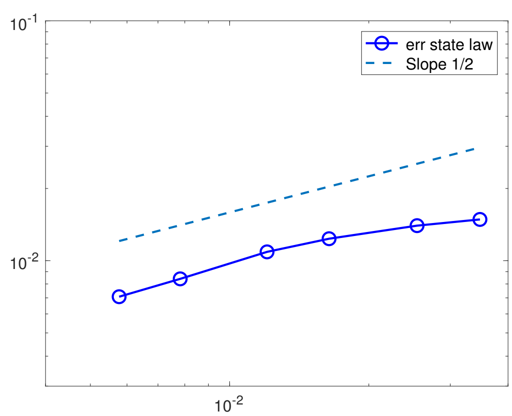

Figure 12: Error on the state equation as a function of h_{max}.

4.3.2 The case without gravity

Finally, we investigate a similar case to the one developped in section 4.3.1, but without any gravity field (Ra = 0). In such a simple configuration, the exact solution is known and given by:

$$\mathbf{u}_{\mathbf{ex}}(x,y) = 0,\ T_{\text{ex}} = T_h + (T_h - T_c)\,x,\ P_{\text{ex}} = P_0,\ \rho_{\text{ex}} = \frac{P_0}{R\,T_{\text{ex}}} \text{ and } \ \pi_{\text{ex}} = 0. \tag{47}$$

We aim to investigate the behaviour of the scheme from a small perturbation around this steady state. As expected, we observe that if the computation is initialized using the exact solution (47), the fluid remains at rest and the exact solution is preserved, as it was the case for the constant states test in subsection 4.1.1. Then, we start the computation by using $\rho^{\eta}_{\text{init}}$ and T^{η}_{init} instead of ρ_{ex} and T_{ex} respectively given by:

$$\rho^{\eta}_{\text{init}} = \rho_{\text{ex}} + \eta\ \sin(2k\pi x)\sin(2k\pi y) \quad \text{ and } \quad T^{\eta}_{\text{init}} = \frac{P_0}{R\,\rho^{\eta}_{\text{init}}},$$

with $\eta = 0.01$ and $k = 3$. Time iterations are performed until the relative residual on all the variables is less than 10^{-10}, leading to the numerical steady state $\mathbf{u}_h^{(s)}, T_h^{(s)}, P^{(s)}, \rho_h^{(s)}$ and $\pi_h^{(s)}$. If we compare the solution obtained with the unperturbed steady state (47), we observe that the $L^2(\Omega)$ norms of the difference between the unperturbed state (47) and the numerical steady one for the velocity, the temperature and the dynamic pressure are less than 10^{-10} whatever the mesh used, concluding that the state (47) is reached for these variables. Since the finite volume method ensures the mass preservation, the quadrature error made at initial time to evaluate the mass implies the mesh to be refined in order to ensure the convergence of $\rho_h^{(s)}$ and $P^{(s)}$ towards ρ_{ex} and P_{ex} respectively. We display in Figure 13 the relative errors on the density, the thermodynamic pressure and the state equation. It can be observed that all these quantities tend towards zero as expected, and that the convergence is faster for $P^{(s)}$ than for $\rho^{(s)}$.

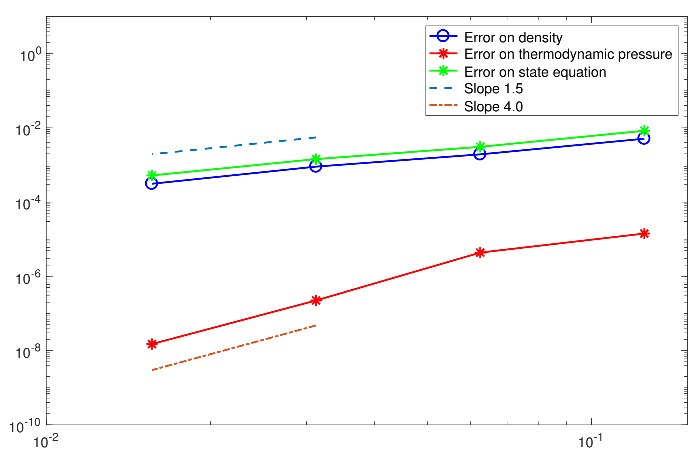

Figure 13: $\dfrac{||\rho_h^{(s)} - \rho_{\text{ex}}||_{L^2(\Omega)}}{||\rho_{\text{ex}}||_{L^2(\Omega)}}$, $\dfrac{|P^{(s)} - P_{\text{ex}}|}{|P_{\text{ex}}|}$ and $\Big|\Big|\rho_h^{(s)} - \dfrac{P^{(s)}}{RT_h^{(s)}}\Big|\Big|_{L^2(\Omega)}$ versus h_{max}.

5 Conclusion

In this paper, a combined Finite Volume - Finite Element method based on a time splitting has been developed. The main ingredients are:

- to solve the mass conservation equation by a FV method instead of exploiting the equation of state;
- to solve the temperature and the momentum equations by a FE method, using a projection method in order to fulfill the constraint (16);
- to keep a particular definition of the velocity (see (39)) in order to verify the divergence constraint also in the FV scheme.

We compared the numerical results of the proposed method with those obtained implementing one of the schemes proposed in [2]. We checked that the C-FV-FE scheme allows to preserve the constant states as well as the maximum principle on the density at the incompressible limit of the fluid, and gives the optimal rates of convergence on a smooth benchmark using an analytical solution. We then investigated a problem of injection of hot gas into a cavity filled with the same gas, obtaining results very similar to those reported in the literature, and observing that a fixed-point iterations procedure is not necessary, even if it can increase the convergence process. Finally, we simulated a fluid subject to the natural convection in a cavity, for which high temperature gradients are involved in the vicinity of the boundaries. Once again, the developped scheme provided satisfactory qualitative results as well as convergence rates.

Acknowledgements

This work was supported in part by the Labex CEMPI (ANR-11-LABX-0007-01).

A Appendix

In this section, we will detail the fixed-point iterations algorithm. We perform a loop of index l. Knowing $P^{n+1,l}$, $T^{n+1,l}$, $\mathbf{u}^{n+1,l}$ and $\pi^{n+1,l}$, we show how to compute $P^{n+1,l+1}$, $T^{n+1,l+1}$, $\mathbf{u}^{n+1,l+1}$ and $\pi^{n+1,l+1}$. Note that for a generic variable a, $a^{n+1,0} = a^n$.

1. The thermodynamic pressure $P^{n+1,\,l+1}$ is computed by the global mass conservation:

$$P^{n+1,\,l+1} = \frac{\gamma - 1}{\gamma} \left(\int_\Omega \rho^{n+1,l} \right) \left(\int_\Omega \frac{1}{T^{n+1,l}} \right)^{-1}.$$

2. The time derivative of the thermodynamic pressure $\left(\dfrac{\mathrm{d}P}{\mathrm{d}t}\right)^{n+1,l+1}$ is computed by solving (17):

$$\begin{aligned}\left(\frac{\mathrm{d}P}{\mathrm{d}t}\right)^{n+1,l+1} + \frac{\gamma P^{n+1,l+1}}{|\Omega|}\int_{\partial\Omega}\mathbf{u}_D^{n+1}.\mathbf{n} &= \frac{\gamma-1}{|\Omega|\mathrm{Re}\,\mathrm{Pr}}\int_{\partial\Omega_D}\nabla(T^{n+1,l})\cdot\mathbf{n}\\ &+\frac{\gamma-1}{|\Omega|\mathrm{Re}\,\mathrm{Pr}}\int_{\partial\Omega_N}F_N^{n+1}.\end{aligned}$$

3. The new density $\rho^{n+1,l+1}$ is computed by solving:

$$\begin{aligned}\frac{\hat{\rho}^{n+1,l+1}-\rho^n}{\Delta t}+\nabla\cdot(\rho^n\mathbf{u}^{n+\frac{1}{2},l}) &= 0,\\ \frac{\rho^{n+1,l+1}-\rho^n}{\Delta t}+\frac{1}{2}\left(\nabla\cdot(\rho^n\mathbf{u}^{n+\frac{1}{2},l})+\nabla\cdot(\hat{\rho}^{n+1,l+1}\mathbf{u}^{n+\frac{1}{2},l})\right) &= 0,\end{aligned}$$

with:

$$\mathbf{u}^{n+\frac{1}{2},l}=\frac{\mathbf{u}^n+\mathbf{u}^{n+1,l}}{2}.$$

4. The temperature $T^{n+1,l+1}$ is computed by solving:

$$\begin{aligned}&\rho^{n+1,l+1}\left(\frac{3T^{n+1,l+1}-4T^n+T^{n-1}}{2\,\Delta t}+\mathbf{u}^{n+1,l}\cdot\nabla T^{n+1,l+1}\right)\\ &\quad-\frac{3P^{n+1,l+1}-4P^n+P^{n-1}}{2\,\Delta t}-\frac{1}{\mathrm{Re}\,\mathrm{Pr}}\Delta T^{n+1,l+1}=0,\end{aligned}$$

5. The velocity $\mathbf{u}^{n+1,l+1}$ and the pressure $\pi^{n+1,l+1}$ are computed by solving:

$$\begin{aligned}&\rho^{n+1,l+1}\left(\frac{3\mathbf{u}^{n+1,l+1}-4\mathbf{u}^n+\mathbf{u}^{n-1}}{2\,\Delta t}+\mathbf{u}^{n+1,l}\cdot\nabla\mathbf{u}^{n+1,l+1}\right)+\nabla\pi^{n+1,l+1}\\ &\quad-\frac{1}{\mathrm{Re}}\nabla\cdot\boldsymbol{\tau}^{n+1,l+1}=-\frac{1}{\mathrm{Fr}^2}\rho^{n+1,l+1}\,\mathbf{e}_y,\\ &\nabla\cdot\mathbf{u}^{n+1,l+1}=-\frac{1}{\gamma\,P^{n+1,l+1}}\left(\frac{\mathrm{d}P}{\mathrm{d}t}\right)^{n+1,l+1}+\frac{\gamma-1}{\gamma\,\mathrm{Re}\,\mathrm{Pr}\,P^{n+1,l+1}}\Delta T^{n+1,l},\end{aligned}$$

with

$$\nabla\cdot\boldsymbol{\tau}^{n+1,l+1}=\Delta\mathbf{u}^{n+1,l+1}+\frac{1}{3}\nabla\left(\nabla\cdot\mathbf{u}^{n+1,l}\right).$$

References

[1] M. Avila, J. Principe, and R. Codina. A finite element dynamical nonlinear subscale approximation for the low Mach number flow equations. *J. Comput. Phys.*, 230(22):7988–8009, 2011.

[2] A. Beccantini, E. Studer, S. Gounand, J.-P. Magnaud, T. Kloczko, C. Corre, and S. Kudriakov. Numerical simulations of a transient injection flow at low Mach number regime. *Internat. J. Numer. Methods Engrg.*, 76(5):662–696, 2008.

[3] C. Calgaro, E. Chane-Kane, E. Creusé, and T. Goudon. L^∞-stability of vertex-based MUSCL finite volume schemes on unstructured grids: simulation of incompressible flows with high density ratios. *J. Comput. Phys.*, 229(17):6027–6046, 2010.

[4] C. Calgaro, E. Creusé, and T. Goudon. An hybrid finite volume-finite element method for variable density incompressible flows. *J. Comput. Phys.*, 227(9):4671–4696, 2008.

[5] C. Calgaro, E. Creusé, and T. Goudon. Modeling and simulation of mixture flows: application to powder-snow avalanches. *Comput. & Fluids*, 107:100–122, 2015.

[6] Caterina Calgaro, Emmanuel Creusé, Thierry Goudon, and Stella Krell. Simulations of non homogeneous viscous flows with incompressibility constraints. *Math. Comput. Simulation*, 137:201–225, 2017.

[7] A. J. Chorin. Numerical solution of the Navier-Stokes equations. *Math. Comp.*, 22:745–762, 1968.

[8] A. J. Chorin. On the convergence of discrete approximations to the Navier-Stokes equations. *Math. Comp.*, 23:341–353, 1969.

[9] P. G. Ciarlet. *The finite element method for elliptic problems*. North-Holland Publishing Co., Amsterdam-New York-Oxford, 1978. Studies in Mathematics and its Applications, Vol. 4.

[10] S. Dellacherie. On a diphasic low Mach number system. *M2AN Math. Model. Numer. Anal.*, 39(3):487–514, 2005.

[11] S. Dellacherie. On a low Mach nuclear core model. In *Congrès National de Mathématiques Appliquées et Industrielles*, volume 35 of *ESAIM Proc.*, pages 79–106. EDP Sci., Les Ulis, 2011.

[12] S. Dellacherie, J. Jung, P. Omnes, and P.-A. Raviart. Construction of modified Godunov-type schemes accurate at any Mach number for the compressible Euler system. *Math. Models Methods Appl. Sci.*, 26(13):2525–2615, 2016.

[13] V. Gravemeier and W. A. Wall. An algebraic variational multiscale-multigrid method for large-eddy simulation of turbulent variable-density flow at low Mach number. *J. Comput. Phys.*, 229(17):6047–6070, 2010.

[14] V. Gravemeier and W. A. Wall. Residual-based variational multiscale methods for laminar, transitional and turbulent variable-density flow at low Mach number. *Internat. J. Numer. Methods Fluids*, 65(10):1260–1278, 2011.

[15] J.-L. Guermond. Un résultat de convergence d'ordre deux en temps pour l'approximation des équations de Navier-Stokes par une technique de projection incrémentale. *M2AN Math. Model. Numer. Anal.*, 33(1):169–189, 1999.

[16] J. L. Guermond, P. Minev, and J. Shen. An overview of projection methods for incompressible flows. *Comput. Methods Appl. Mech. Engrg.*, 195(44-47):6011–6045, 2006.

[17] J.-L. Guermond and L. Quartapelle. Calculation of incompressible viscous flows by an unconditionally stable projection FEM. *J. Comput. Phys.*, 132(1):12–33, 1997.

[18] J.-L. Guermond and L. Quartapelle. On stability and convergence of projection methods based on pressure Poisson equation. *Internat. J. Numer. Methods Fluids*, 26(9):1039–1053, 1998.

[19] J.-L. Guermond and A. Salgado. A splitting method for incompressible flows with variable density based on a pressure Poisson equation. *J. Comput. Phys.*, 228(8):2834–2846, 2009.

[20] J.-L. Guermond and A. J. Salgado. Error analysis of a fractional time-stepping technique for incompressible flows with variable density. *SIAM J. Numer. Anal.*, 49(3):917–944, 2011.

[21] J. L. Guermond and J. Shen. On the error estimates for the rotational pressure-correction projection methods. *Math. Comp.*, 73(248):1719–1737 (electronic), 2004.

[22] H. Guillard and C. Viozat. On the behaviour of upwind schemes in the low Mach number limit. *Comput. & Fluids*, 28(1):63–86, 1999.

[23] R. Herbin, J.-C. Latché, and K. Saleh. Low Mach number limit of a pressure correction MAC scheme for compressible barotropic flows. In *Finite volumes for complex applications VIII—methods and theoretical aspects*, volume 199 of *Springer Proc. Math. Stat.*, pages 255–263. Springer, Cham, 2017.

[24] V. Heuveline. On higher-order mixed FEM for low Mach number flows: application to a natural convection benchmark problem. *Internat. J. Numer. Methods Fluids*, 41(12):1339–1356, 2003.

[25] P. Le Quéré, R. Masson, and P. Perrot. A Chebyshev collocation algorithm for 2d non-Boussinesq convection. *Journal of Computational Physics*, 103:320–335, 1992.

[26] P. Le Quéré, C. Weisman, H. Paillère, J. Vierendeels, E. Dick, R. Becker, M. Braack, and J. Locke. Modelling of natural convection flows with large temperature differences: a benchmark problem for low Mach number solvers. I. Reference solutions. *M2AN Math. Model. Numer. Anal.*, 39(3):609–616, 2005.

[27] B. Lessani and M. V. Papalexandris. Time-accurate calculation of variable density flows with strong temperature gradients and combustion. *J. Comput. Phys.*, 212(1):218–246, 2006.

[28] P.-L Lions. *Mathematical topics in fluid mechanics. Vol. 2*, volume 10 of *Oxford Lecture Series in Mathematics and its Applications*. The Clarendon Press, Oxford University Press, New York, 1998. Compressible models, Oxford Science Publications.

[29] W. Liu and G. Makhviladze. An implicit finite element solution of thermal flows at low Mach number. *J. Comput. Phys.*, 227(5):2743–2757, 2008.

[30] H. Luo, Baum J.D., and R. Lohner. Extension of harten-lax-van leer scheme for flows at all speeds. *AIAA Journal*, 43(6):1160–1166, 2005.

[31] A. Majda and J. Sethian. The derivation and numerical solution of the equations for zero Mach number combustion. *Combustion Science and Technology*, 42:185–205, 1985.

[32] M. J. Martinez and D. K. Gartling. A finite element method for low-speed compressible flows. *Comput. Methods Appl. Mech. Engrg.*, 193(21-22):1959–1979, 2004.

[33] C.-D. Munz, S. Roller, R. Klein, and K. J. Geratz. The extension of incompressible flow solvers to the weakly compressible regime. *Comput. & Fluids*, 32(2):173–196, 2003.

[34] F. Nicoud. Conservative high-order finite-difference schemes for low-Mach number flows. *J. Comput. Phys.*, 158(1):71–97, 2000.

[35] S. Noelle, G. Bispen, K. R. Arun, M. Lukáčová-Medviďová, and C.-D. Munz. A weakly asymptotic preserving low Mach number scheme for the Euler equations of gas dynamics. *SIAM J. Sci. Comput.*, 36(6):B989–B1024, 2014.

[36] Yohan Penel, Stephane Dellacherie, and Bruno Després. Coupling strategies for compressible-low Mach number flows. *Math. Models Methods Appl. Sci.*, 25(6):1045–1089, 2015.

[37] J. Principe and R. Codina. A stabilized finite element approximation of low speed thermally coupled flows. *International Journal of Numerical Methods for Heat and Fluid Flow*, 18:835–867, 2007.

[38] J. Principe and R. Codina. Mathematical models for thermally coupled low speed flows. *Advances in Theoretical and Applied Mechanics 2*, pages 93–112, 2009.

[39] R. Temam. *Navier-Stokes equations. Theory and numerical analysis*. North-Holland Publishing Co., Amsterdam-New York-Oxford, 1977. Studies in Mathematics and its Applications, Vol. 2.

[40] E. Turkel. Preconditioned methods for solving the incompressible and low speed compressible equations. *Journal of Computational Physics*, 72:277–298, 1987.

[41] A. Tyliszczak and H. Deconinck. Application of time preconditioning and high-order compact discretization method for low Mach number flows. *Internat. J. Numer. Methods Fluids*, 72(6):650–670, 2013.

[42] D. Vigneron, J.-M. Vaassen, and J.-A. Essers. An implicit finite volume method for the solution of 3D low Mach number viscous flows using a local preconditioning technique. *J. Comput. Appl. Math.*, 215(2):610–617, 2008.

[43] K. N. Volkov and A. G. Karpenko. Preconditioning of gas dynamics equations in compressible gas flow computations at low Mach numbers. *Comput. Math. Math. Phys.*, 55(6):1051–1067, 2015.